The effect of Pliocene regional climate changes on silicate weathering: a potential amplifier of Pliocene-Pleistocene cooling

Pierre Maffre[1], John C. H. Chiang[1], and Nicholas L. Swanson-Hysell[1]

[1]University of California, Berkeley

Correspondence: Pierre Maffre (maffre@berkeley.edu)

Abstract.

The warmer early Pliocene climate featured changes to global sea surface temperature (SST) patterns, namely a reduction to the equator-pole gradient and to the east-west SST gradient in the tropical Pacific, the so-called "permanent El Niño". Here we investigate the consequences of the SST changes to silicate weathering and thus to atmospheric CO_2 on geological
5   timescales. Different SST patterns than today imply regional modifications of the hydrological cycle that directly affects continental silicate weathering in particular over tropical "hotspots" of weathering such as the Maritime continent, thus leading to a "weatherability pattern effect". We explore the impact of Pliocene SST changes on weathering using climate model and silicate weathering model simulations, and deduce CO_2 and temperature at C cycle equilibrium between solid Earth degassing and silicate weathering. In general, we find large regional increases and decreases to weathering fluxes that largely cancel out
10   one another. For permanent El Niño conditions, weathering decreases outweigh the increases, leading to a small amplification of warming relative to the present-day by $0.4\,°C$. The demise of permanent El Niño could have had a small amplifying effect on cooling from the early Pliocene into the Pleistocene. For the reduced equator-pole gradient, the weathering increases and decreases largely cancel leading to no detectable difference in global temperature at C cycle equilibrium.

1 Introduction

15   Evidence has been accumulating that east-west (zonal) gradients of sea surface temperature (SST) and thermocline depth in the tropical Pacific were reduced during the warm early Pliocene $(4.5-3\,\text{Ma})$ with respect to modern conditions (e.g., Cannariato and Ravelo, 1997; Ravelo, 2004; Wara et al., 2005; Fedorov et al., 2013). These features, resembling modern El Niño events, have led to the idea of a "permanent El Niño" climatic state during the Pliocene epoch, also named "El Padre" (Shukla et al., 2009). Paleoclimate proxy data also supports that the average equator-pole (meridional) temperature gradient was reduced
20   during the warm early Pliocene (Brierley et al., 2009; Brierley and Fedorov, 2010; Fedorov et al., 2013).

The transition between early Pliocene to modern climate conditions is thought to be linked to global cooling from the Pliocene (5.3 to 2.6 Ma) into the Pleistocene (2.6 to 0.01 Ma), both as a cause or a consequence. Molnar and Cronin (2015) argued that the onset of a modern tropical Pacific zonal SST gradient (due to the larger cooling of the eastern tropical Pacific) may have permitted the inception of the Laurentide ice sheet. In this hypothesis, teleconnection altered the atmospheric
25   circulation over North America thereby enabling accumulation of perennial snow in winter in northern North America. The

authors developed the hypothesis that vigorous modern Pacific Walker circulation – which enhanced the zonal SST gradient – was caused by the restriction of the Indonesian seaway as well as the increased land area of emerged islands in the Maritime Continent, both due to tectonic processes associated with arc-continent collision. On the other hand, Fedorov et al. (2006) proposed a feedback loop where shoaling of the thermocline with cooling climate activates the Bjerknes feedback and thus in-

30 vigorates the Walker circulation, further enhancing climate cooling through cloud-albedo and ice-albedo feedback. The zonal tropical Pacific SST gradient has also been shown to be linked to the global meridional temperature gradient (Fedorov et al., 2015). Therefore, all the following elements, strengthening zonal and meridional gradients, intensification of El Niño Southern Oscillation (ENSO), onset of a mean climate state closer to La Niña, and global cooling, would be part of a same process.

One element that has been largely overlooked in these considerations about regional climate changes is their effect on silicate

35 weathering and the silicate weathering feedback. The so-called silicate weathering paleothermostat (Walker et al., 1981) is the hypothesis that long-term climate is controlled by the balance between deep earth degassing of CO_2 and its consumption by continental silicate weathering and associated oceanic carbonate precipitation (the Urey reaction, Urey, 1952). Weathering reactions are enhanced by warmer climate which introduces a negative feedback: atmospheric CO_2 is stabilized at the level where its consumption balances its degassing (Walker et al., 1981; Berner et al., 1983). Continental runoff rate is a key factor

40 controlling silicate weathering rate (Gaillardet et al., 1999; Dessert et al., 2003; Oliva et al., 2003; Maher and Chamberlain, 2014). The very existence of the silicate weathering paleothermostat relies to a large extent on the fact that runoff rates, on average, increase with rising CO_2 and associated global warming. Hence, processes that affect the distribution of continental runoff, even without direct effects on global temperature, have the potential to change the efficiency of silicate weathering, and therefore, equilibrium atmospheric CO_2 level, and global temperature. This phenomenon is analogous to the so-called "pattern

45 effect" (Langenbrunner, 2020) in the Earth's temperature climate sensitivity to atmospheric CO_2. As with climate sensitivity, SST patterns may have significant effects on the efficiency of silicate weathering – hereafter called "weatherability" – because they affect atmospheric convection, precipitation and runoff.

In that regard, reducing meridional or zonal SST gradients (with respect to modern climate) may decrease global weatherability by shifting rainfall away from tropical land masses. In the case of meridional gradient, Burls and Fedorov (2017)

50 suggested a reduced equatorward moisture transport by the Hadley circulation with flatter SST gradient. In the case of zonal gradient, a weaker Pacific gradient should lead to reduced Pacific Walker circulation, that is responsible of intense precipitation over the Maritime continent in modern climate. Indeed, El Niño events, where the Pacific Walker circulation collapses, leads to a drastic decrease of continental runoff on the Maritime continent, as well as most of South America near the equator (see Fig. 1 showing the El Niño-years climatology of precipitation and runoff). On average, runoff is reduced by $\sim 3\%$ on land during

55 El Niño-years. The key element here is that some tropical areas that are drier in El Niño years, are known hotspots of silicate weathering – mainly, the Southeast Asian Islands known as the Maritime continent (Figs. 1 and 2). Another contribution to changes in silicate weathering should be expected from the Himalaya and the portion of the Andes north of the equator, that also experience decreases in runoff during El Niño years.

The above text and associated hypothesis can be summarized as: "With weaker meridional and zonal temperature gradients,

60 the decrease of runoff over land, specifically on tropical weathering hotspots, would lead to reduced weatherability and, as a
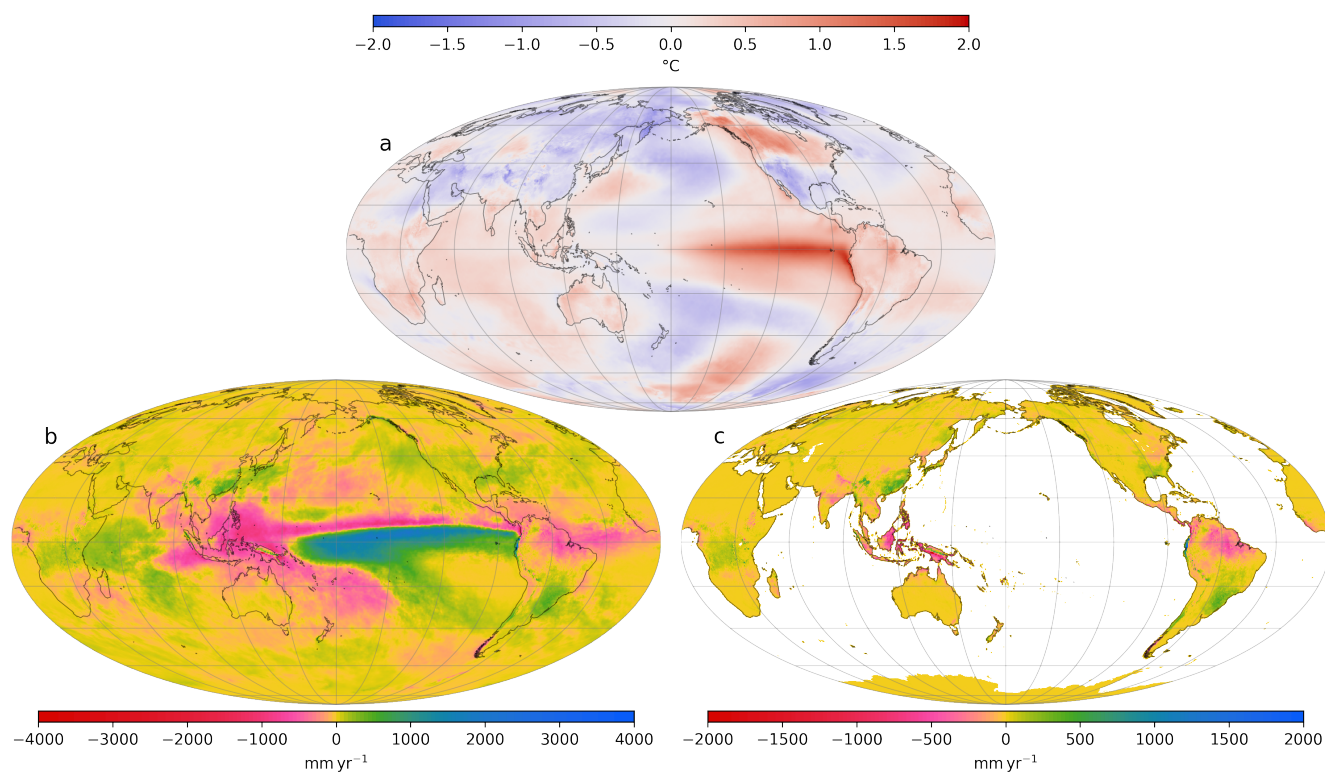
Figure 1. Differences in climatology associated with El Niño years. (a): anomaly of $2\,\mathrm{m}$ temperature, average of El Niño years (May to following April) minus the full climatology average, data from ERA5 reanalysis (see Methods, section 2.2 for details). The maps are Mollweide projections with graticules plotted every $30\,°$ of longitude and every $20\,°$ of latitude (both starting from $0\,°$). (b): same El Niño anomaly as in (a) for total precipitation. (c): same El Niño anomaly as (a) for continental runoff. Note that it is significantly drier over the South-East Asian Islands in El Niño years with more precipitation falling over the tropical Pacific ocean rather than over land.

result, higher CO_2 levels contributing to the warmer Pliocene climate." If we further assume that colder climate favors stronger meridional and zonal gradients, the overall process of cooling would act as a positive feedback loop where increased cooling leads to increased precipitation on key land masses, which would lead to enhanced weatherability and increased cooling. This process has the potential to have amplified climate cooling from the warm early Pliocene into the Pleistocene.

65   In this contribution, we investigate the potential effect of meridional and zonal gradients on global climate through the silicate weathering feedback, without seeking to determine the cause of these regional climate features. We first provide an estimation of the silicate weathering anomaly using the climate fields from ERA5 reanalysis 1979–2020 (Muñoz Sabater, J., 2019; Hersbach et al., 2019), with the assumption that the average climate of El Niño events is a good representation of Pliocene permanent El Niño. This method enables a qualitative assessment of whether the effect of a permanent El Niño state

70   on global chemical weathering would generate a warmer or colder global climate (because of a decrease or an increase of chemical weathering, respectively). However, one cannot quantitatively estimate this warming or cooling because the climate

reanalysis only exist at current CO_2 levels, yet, if silicate weathering is disturbed, CO_2 will adjust to restore the carbon cycle balance between CO_2 degassing and its consumption by silicate weathering. On the million-years timescale of Pliocene to modern, it is this equilibrium CO_2 level that matters for climate evolution. Furthermore, it is possible that the average of El
75 Niño years is not a perfect analog of a permanent El Niño, because of the transient nature of those events, and the fact that they are not bound to radiative balance, as is a long-term equilibrium climate state.

For these two reasons, we designed numerical climate experiments aimed at reproducing Pliocene climate features with a climate model, focusing on the meridional and the zonal tropical SST gradient. Doing so, we provide a quantitative estimation of the role of a "weatherability pattern effect" on climate evolution since the warm early Pliocene, through the silicate
80 weathering feedback.

2 Methods

2.1 Silicate weathering model

We use the silicate weathering model published in Park et al. (2020). This model represents the steady-state vertical profile of primary silicate minerals abundance in a regolith – the interface between unweathered bedrock and land surface. Minerals are
85 progressively weathered until they are removed from the regolith through physical erosion of the surface. Hence, weathering profiles show a continuous depletion of primary minerals from bedrock to the surface. The vertically-integrated weathering rate depends on the rate of physical erosion (which leads to upward advection of primary minerals), the efficiency of weathering chemical reactions (that depend on runoff and temperature), and the residence time of minerals in the regolith (that is also controlled by erosion rate). The derivation of this model was carried out by Gabet and Mudd (2009) and West (2012), who
90 parameterized the climatic control of weathering reactions (through temperature and runoff). The erosion rate is computed as a power-law of topographic slope and runoff rate (Maffre et al., 2018; Park et al., 2020).

The value of interest computed by the weathering model is the amount of dissolved Ca and Mg released by weathering of silicates minerals (integrated over the regolith profile). This flux corresponds to long-term CO_2 consumption in the geological carbon cycle through the eventual precipitation of marine carbonates. The weathering model is applied on every point of the
95 continental mesh grid, at the resolution of the climate fields used (see following sections). On each point, computation of the estimated weathering rate is done for 5 lithological classes of silicates (as in Park et al., 2020) that are simplified from the global lithological map of Hartmann and Moosdorf (2012). The slope field was derived from the elevation dataset of the Shuttle Radar Topography Mission (Farr et al., 2007) at 30" resolution. Both the lithological classes and the slope were interpolated on the desired mesh grids.

100 The model parameters are taken from Park et al. (2020) who provided an ensemble of 573 "best-fit" unique parameter combinations resulting from a comparison of model results to modern chemical weathering fluxes across watersheds. Similarly to Park et al. (2020), the weathering model is run with all those unique parameter combinations. We present, for each model run, the ensemble of results (e.g., the ensemble of the global weathering flux). This approach allows us to quantify the uncertainties arising from the weathering parameters.

2.2 Climate reanalysis and selection of El Niño and La Niña years

The reanalysis climate fields used in this study are from ERA5-land 1981–2019 (Muñoz Sabater, J., 2019) for continental runoff, and ERA5 1979–2020 (Hersbach et al., 2019) for $2\,\mathrm{m}$ temperature and SST. The monthly averaged fields at the native resolution ($0.1\,°$ for ERA5-land and $0.25\,°$ for ERA5) were interpolated on a longitude-latitude grid of $0.5\,°$ resolution.

To determine the climatology associated with El Niño and La Niña years, we generate an interannual index of ENSO, and then use it to create composite El Niño and La Niña years. The generation of the index proceeded as follows: we used the detrended monthly SST average on Niño 3 region, that is $5\,°\mathrm{N}$–$5\,°\mathrm{S}$, $150\,°$–$90\,°\mathrm{W}$ (Trenberth and Stepaniak, 2001). We detrended the time-series by performing a linear regression with respect to time, and subtracted the "time" term from the original time-series. We grouped the monthly time-series in "year" vectors of 12 elements, corresponding to the 12 months, from May to April of the next calendar year. We subtracted to each year vector the average of all years, to center the vectorial time-series. We then performed a principal component analysis. We identified the first eigenvector (or EOF, for empirical orthogonal function) as the signature of El Niño events. We projected the detrended, centered, vectorial time-series on this first EOF (scalar product of the two 12 elements vectors, for each year). We normalized the scalar time-series obtained in this way by dividing it by its standard deviation (across the years). This normalized time-series can be interpreted as a time-series of the El Niño index for each year. We selected the El Niño years as the years having an index > 0.9, and < -0.9 for the La Niña years.

Based on the described procedure, we selected the years 1982, 1987, 1991, 1997, 2009 and 2015 as El Niño years, and the years 1984, 1988, 1999, 2007 and 2010 La Niña years (in each case, from May to April of the next calendar year).

2.3 Climate model

For the climate numerical experiments, we used the Community Earth System Model (CESM) version 1.2.2.1. The experiments were conducted using the components CAM4 for the atmospheric dynamics, CLM4.0 land model, CLM4.0 CN river-runoff component, CICE prognostic sea ice, and for the oceanic component, either fixed SSTk DOCN in slab ocean mode, or full ocean model (Parallel Ocean Program version 2). The slab ocean approximates a well-mixed ocean mixed layer with a fixed depth set to the annual mean; an ocean heat transport convergence (i.e., the "Q flux") from a CESM1 pre-industrial fully coupled run is prescribed at each ocean gridpoint to achieve a simulated sea surface temperature close to the pre-industrial. The grids used are a regular $0.9\,° \times 1.25\,°$ (latitude× longitude) for atmosphere and land modules, a regular $0.5\,°$ for runoff routing, and a $\sim 1\,°$ "displaced" grid, with Greenland pole, (0.9x1.25_gx1v6) for the ocean models (both slab and full) and sea ice modules.

All experiments were conducted with permanent 1850 (pre-industrial) boundary conditions, with the exception of the few modifications discussed later in the article, that are atmospheric CO_2 concentration, slab ocean Q flux, and clouds albedo. Experiments were run 40 years for the fixed SST cases, 50 years for the slab ocean cases, and 230 years (170 years for the control) for the coupled ocean-atmosphere cases. All experiments were initiated with a "cold start" (internally-generated initial

Table 1. Summary of all the climate simulations presented in this study

Name	boundary conditions*	ocean model	CO_2 level (ppmv)	integration time
COA-ctrl	pre-industrial	full	284.7	170 yr
COA-Plio	modified cloud albedo	full	284.7	230 yr
fSST-ctrl	pre-industrial	fixed SST	284.7	40 yr
fSST-Plio-full	SST from "COA-Plio"	fixed SST	284.7; 300; 320	40 yr
fSST-Plio-10SN	$10\,°S$–$10\,°N$ SST from "COA-Plio"	fixed SST	284.7; 300	40 yr
control	pre-industrial	slab	213.5; 284.7; 427.1 569.4; 854.1; 1138.8	50 yr
full Pliocene SST	Q flux derived from "fSST-Plio-full"	slab	180; 200; 250 309.4; 427.1	50 yr
$10°SN$ Pliocene SST	Q flux derived from "fSST-Plio-10SN"	slab	200; 250; 299.4 569.4; 854.1	50 yr

* refers to all climate model boundary conditions except atmospheric CO_2. Anything else than the indicated modifications is pre-industrial

condition, corresponding to a pre-industrial climate). In all cases, the last 30 years of the model runs were used to compute the climatology average. Table 1 summarized the specific features of all the climate simulations conducted here.

2.4 Geographic division of silicate weathering

140 To quantify the contributions of the different regions of Earth to the changes of silicate weathering flux due to perturbations of climate fields, we used the geographic division shown in Fig. 2. This division is meant to isolate known weathering hotspots (e.g. Maritime Continent and East African rift), major mountain ranges, and, for the remaining regions, tropics versus subtropics. The boundaries of these regions are somewhat arbitrary, especially for the mountain ranges, and their naming should be considered as a simplification of the broader regions. For instance, "Himalaya" refer to the merging of the Himalayan range,

145 its extension over the Longmen Shan and in South-East Asia, the Tibetan plateau and the Tian Shan. Despite the subjectivity of those boundaries, these divisions give a sense of the different response of individual regions that are useful for summarizing results.

3 Results

3.1 Weathering rates using ERA5 reanalysis

150 #### 3.1.1 Control simulation

We first run the weathering model using ERA5 reanalysis of climate fields (1981–2019 climatology average), as a control simulation. The resulting weathering rates (averaged over the selected parameterizations) are presented in on a map in Fig. 3.
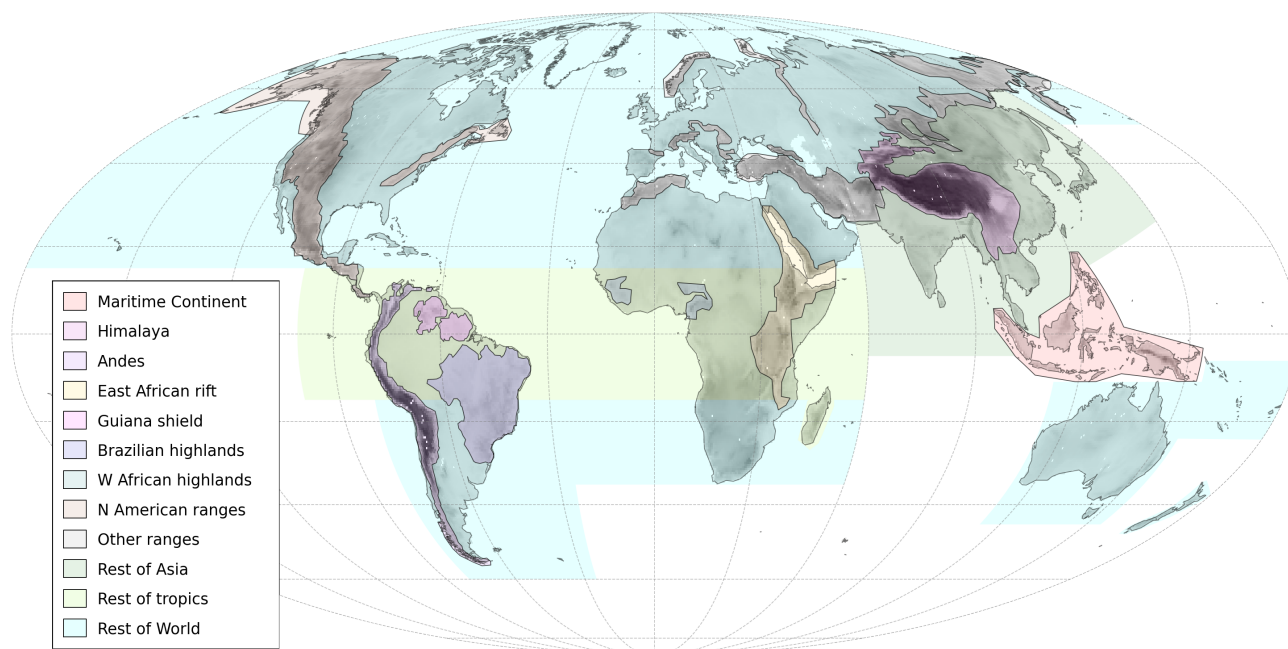
Figure 2. Map of the geographic division used to summarize results in this study (colored semi-transparent shades) superimposed on land topography. The map is a Mollweide projection (equal area) with parallels drawn every $20\,^\circ$ and meridians every $30\,^\circ$, both starting from $0\,^\circ$.

The total CO_2 consumption by weathering is $5.3\,\mathrm{Tmol\,yr^{-1}}$. This control weathering field is very similar to the one published in (Park et al., 2020, Fig. S5 of their contribution), who used the same model, parameter combinations and slope fields, but
155 different climate fields.

The contribution of the different regions of Earth to this control weathering flux is shown in Fig. 4 (blue bars). The weathering flux from the Maritime Continent is about 11% of the total flux, which is consistent with previous estimates (e.g., Molnar and Cronin, 2015). The main mountain belts (broader Himalaya, Andes and North and central American ranges, including the rocky mountains) together contribute to $\sim 22\%$ of the total. Another significant weathering contributor is the East African Rift ($\sim 8\%$
160 of the total), owing to relatively high runoff rates, the substantial amount mafic silicate rocks exposed, and to the relatively steep topography fostering erosion – and hence, chemical weathering. Taiwan and New Zealand, that are known hotspots of erosion rates, do not contribute significantly to the total weathering flux because of the limited areal extent of their orogens.

3.1.2 El Niño and La Niña years climatologies

We then recompute the weathering rates with the same dataset, but keeping only the years of the climate time-series identified as
165 "El Niño" or "La Niña" (average of May to April, see Methods, section 2.2). The anomaly of Earth-integrated weathering flux is $-90 \pm 15.4\,\mathrm{Gmol\,yr^{-1}}$ for El Niño years and $+138 \pm 30.1\,\mathrm{Gmol\,yr^{-1}}$ for La Niña ("$\pm$" denoting the standard deviation of the weathering anomaly over the selected parameterizations). If we extrapolate from the silicate weathering feedback computed
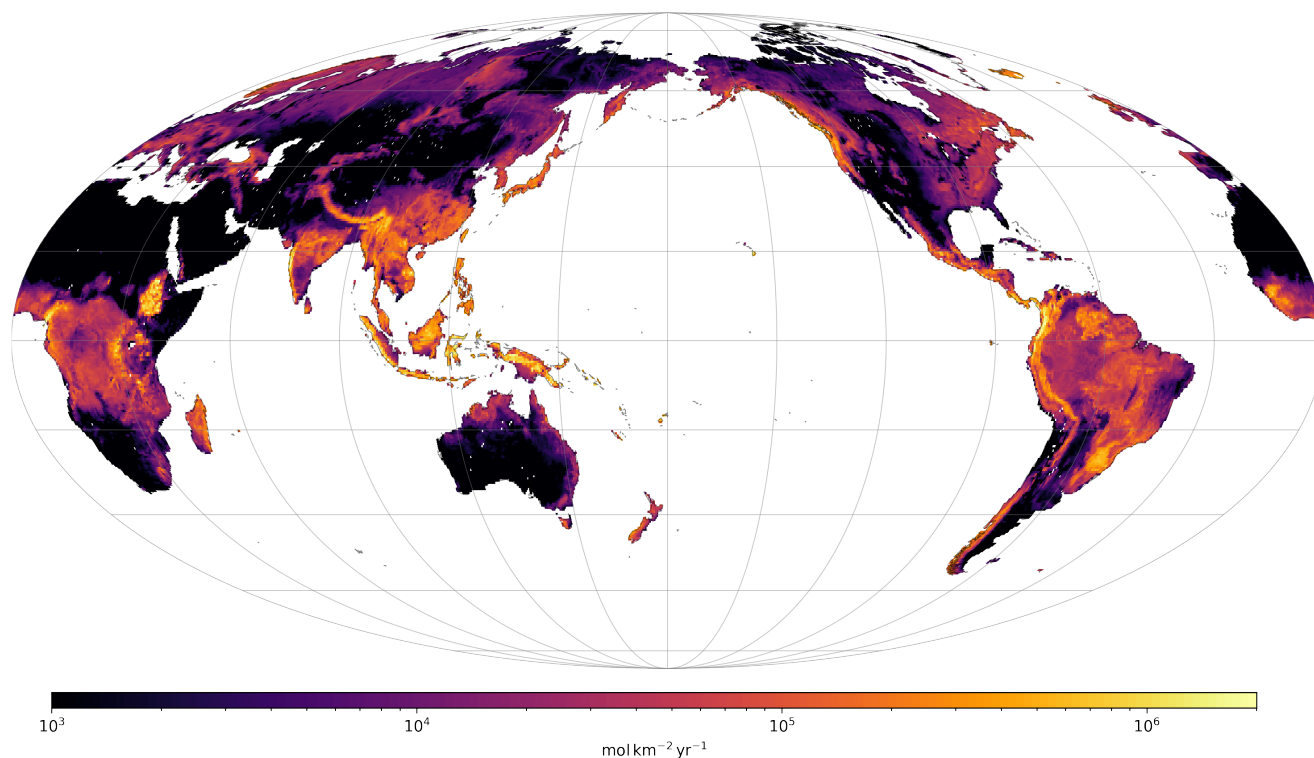
Figure 3. Average chemical weathering rates (Ca and Mg from silicate minerals) over the parameter combinations (i.e., the weathering model is run for each of the 573 selected parameter combination, and the 573 weathering fields are then averaged). Weathering is computed using climate fields from ERA5 reanalysis (climatology average 1981–2019) at $0.5\,°$ of resolution. Map projection and graticules are the same as in Fig. 2.

with CESM climate simulations (see also Fig. 15), these weathering anomalies would correspond to global mean temperature anomalies of $+0.22\,°C$ for the El Niño conditions and $-0.35\,°C$ for La Niña conditions. These relatively small values of
170   weathering anomaly (1.7% and 2.6% of the total control flux, respectively) are the consequences of local increase and decrease of weathering rates that compensate each other (Fig. 5). Nevertheless, the differences from 0 are robust among all the selected parameterizations (the absolute anomaly of weathering flux is ~ 4 times larger than the standard deviation due to the parameter uncertainties), and approximately symmetrical between El Niño and La Niña conditions. These results support our hypothesis of climate cooling caused by the progressive onset of "La Niña-like" mean climatic conditions, though the magnitude of this
175   cooling may not have been substantial.

Local weathering anomalies are largely driven by changes in runoff rates. Many regions display dipolar patterns under El Niño conditions (Fig. 5a). For example, weathering fluxes increase on the Ethiopian Traps associated with El Niño conditions, but decrease on the southern part of the East African rift, they increase on the Andes near the equator, but decrease in the northernmost part of the range, and decrease on the central Himalaya but increase the western part. Hence, the anomaly of
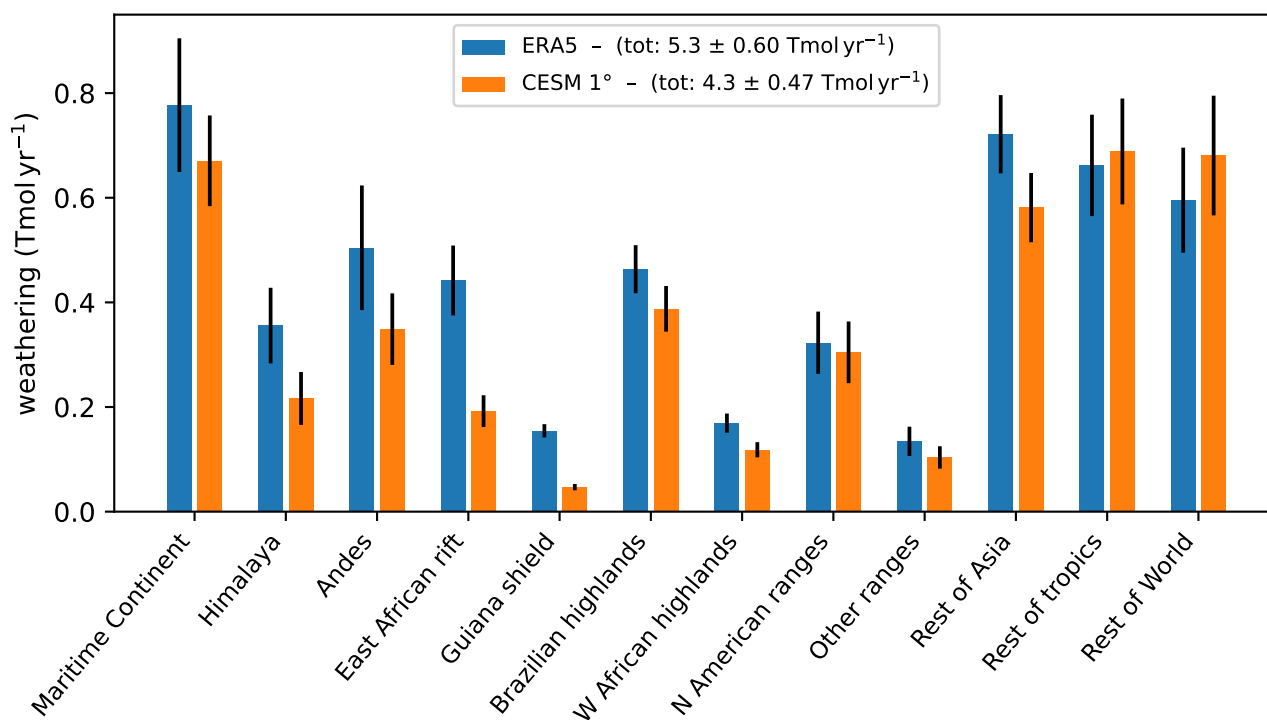
Figure 4. Bar plot of chemical weathering fluxes integrated over the geographic regions shown in Fig. 2, using climate fields from ERA5 reanalysis (1981–2019 average, $0.5\,^{\circ}$ of resolution, blue bars), or CESM1.2 climate model pre-industrial control simulation (with slab ocean model) performed in this study (average of last 30 years simulations, $\sim 1\,^{\circ}$ of resolution, orange bars). The main colored bars denote the average weathering flux of the 573 parameterizations, whereas the black error bars denote the standard deviation over those parameterizations. The total (summed) weathering flux is indicated on the legend box giving both the average and associated standard-deviation resulting from the different weathering model parameterizations.

180 weathering flux integrated over those regions is close to zero (Fig. 6). Most of the negative anomaly of El Niño weathering comes from the Maritime Continent. The weathering integrated over this region is almost equal to the total anomaly (Fig. 6, purple bars). This result highlights the key role this area has potentially played in cooling Earth's climate over the last few million years. The signal from the Maritime Continent is expanded by further weathering decrease on the Deccan Traps and the Guiana highlands associated with El Niño conditions, and partially offset by increase on the Brazilian highlands (Fig. 5

185 and 6).

It is interesting to note that although the sign of weathering anomalies under La Niña conditions is nearly everywhere the opposite of the ones under El Niño conditions, the magnitude of those anomalies is not perfectly symmetrical (Fig. 6).
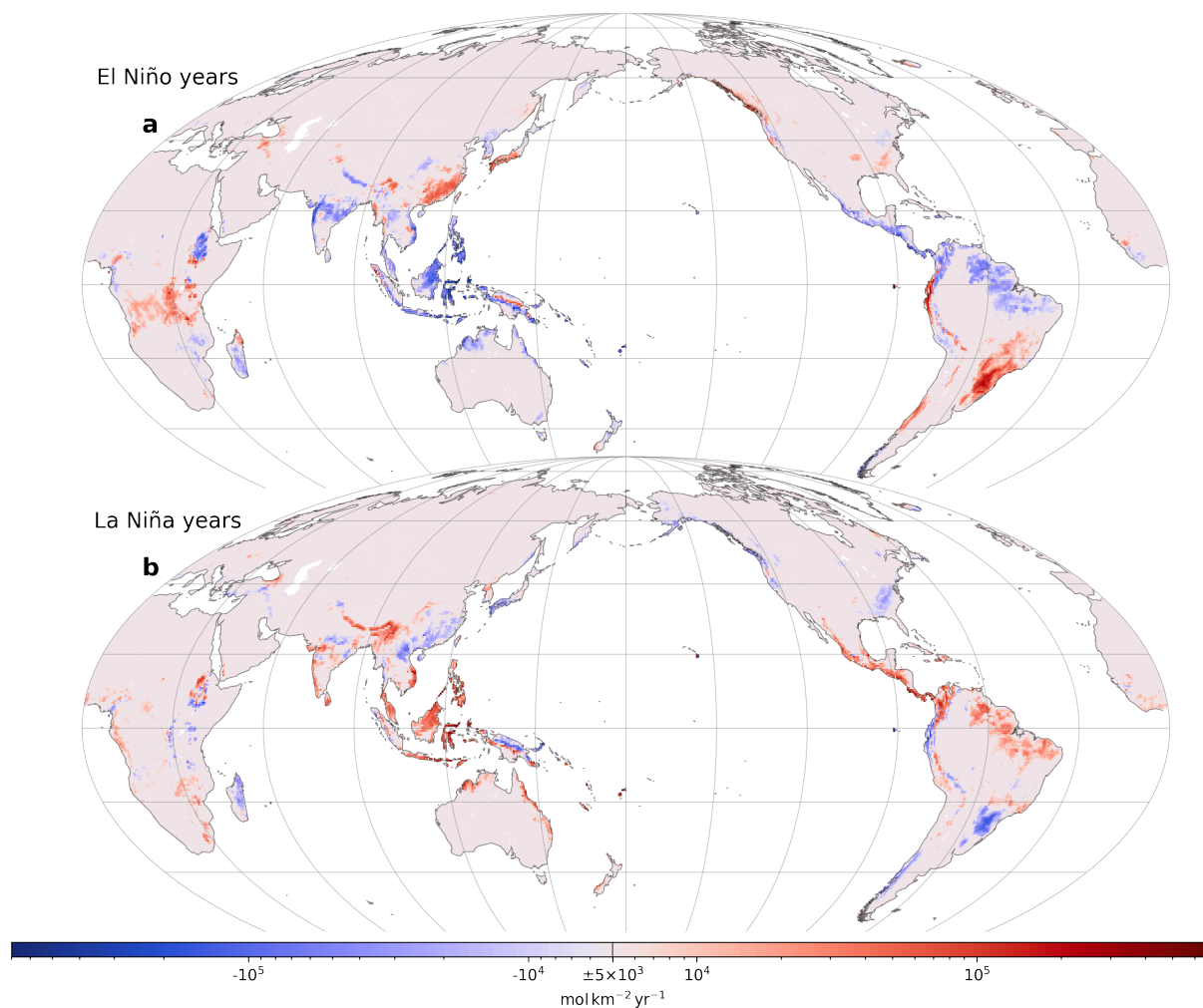
Figure 5. Anomaly of modeled weathering rate with respect to control weathering (i.e., the field displayed in Fig. 3) for a: El Niño years climatology and b: La Niña years climatology. The weathering rate is averaged over the parameter combinations (as in Fig. 3). The colorbar scale is a "symmetric logarithm" and any value lower than $5 \cdot 10^3 \, \mathrm{mol \, km^{-2} \, yr^{-1}}$ (in absolute value) is approximated as 0. Map projection and graticules are as in to Figs. 2 and 3. There are many regional changes of note as discussed in the text. For example, there is enhanced weathering over the Maritime continent during La Niña years relative to El Niño years (see summary in Fig. 6)

3.2 Exploring the consequences of Pliocene SST

We wish here to take a step further and investigate the consequence of Pliocene gradients of SST on silicate weathering and
equilibrium temperature (i.e., the global mean temperature for which silicate weathering balances degassing). We rely here on
the work of Fedorov et al. (2015) demonstrating that the tropical zonal gradient of SST is linked to the meridional gradient of
SST. This result indicates that Pliocene permanent El Niño could be a consequence of weakened meridional gradient. Drawing
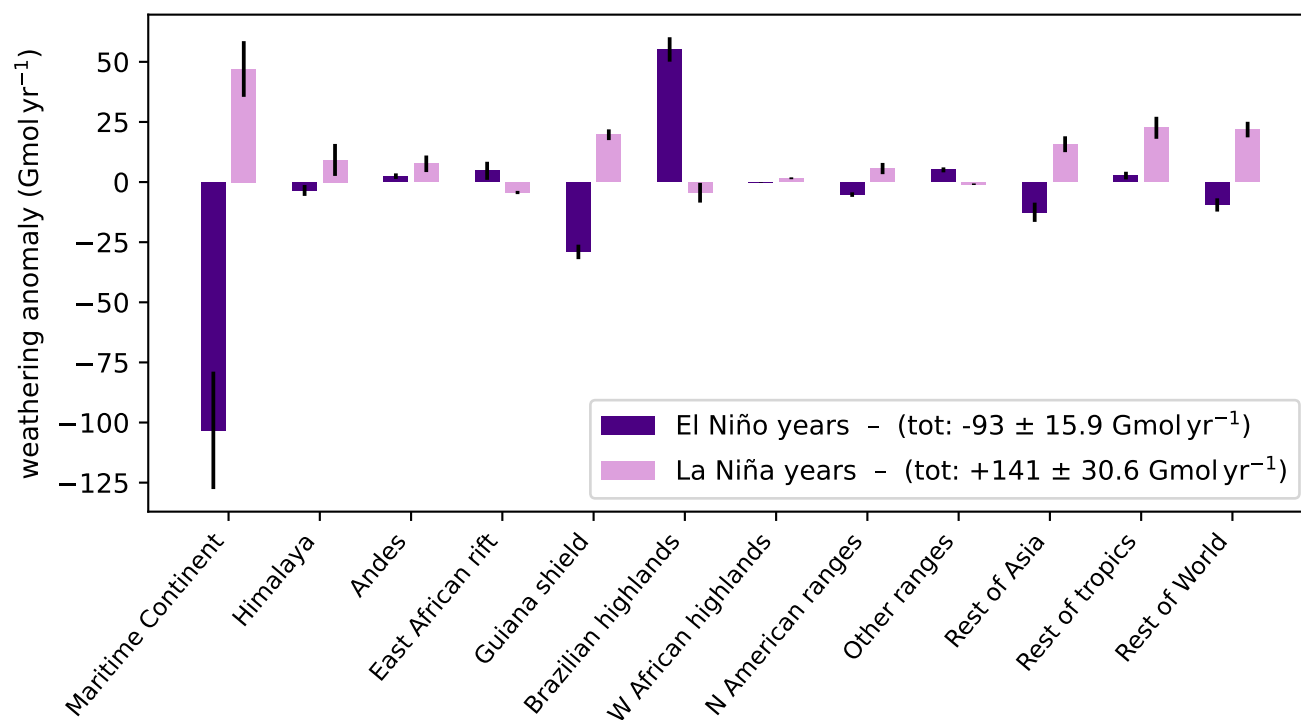
Figure 6. Bar plot of the anomaly of weathering flux integrated over the geographic regions shown in Fig. 2 with respect to ERA5 control weathering (blue bars in Fig. 4) for El Niño or La Niña years climatology, using ERA5 reanalysis. Average (main colored bars) and standard deviation (error bars) refers to the parameterizations, as in Fig. 4. The change in weathering rate is most dramatic over the Maritime Continent due to increased precipitation over land during La Niña years compared to being over the Pacific Ocean during El Niño years

from their work, we designed climate simulations aimed at reproducing Pliocene SST, following the method of Burls and Fedorov (2014).

195   The climate simulations presented in Burls and Fedorov (2014), Fedorov et al. (2015), and Burls and Fedorov (2017) cannot be directly used because the simulations at $0.9\,^{\circ} \times 1.25\,^{\circ}$ of resolution were only conducted at pre-industrial CO_2. However, estimating carbon cycle equilibrium with GEOCLIM necessitates climate simulations at several CO_2 levels. This cannot be done with fixed SST simulations (such as from Fedorov et al., 2015), because it will miss the warming of ocean surface with rising CO_2. On the other hand, changing atmospheric CO_2 in a coupled ocean-atmosphere model at $0.9\,^{\circ} \times 1.25\,^{\circ}$ would

200   require a prohibiting computation time to let the full ocean be at equilibrium with the radiative forcing, and get the correct atmospheric warming. Another issue is that Burls and Fedorov (2014) produced their Pliocene-like SST pattern by altering the cloud properties in the cloud parameterization; as such, the physics of that simulation differs from that of the the pre-industrial control, and thus the two simulations are not directly comparable.

To overcome those difficulties, we designed our simulations in 3 steps. First, we apply the method of Burls and Fedorov

205 (2014) to seeks to reproduce Pliocene SST. In the ocean-atmosphere coupled version of CESM1.2, we modified the cloud visible albedo by changing the value of the water path in the radiative code of CAM4. The cloud liquid and solid water path multiplied by 3.4 between 15 °N North and South, and the cloud liquid water path multiplied by 0.4 in the rest of the Earth. We ran those simulations for 230 years, which is sufficient for the surface ocean to respond to the perturbation (Fedorov et al., 2015). At this point, we are not interested in accurately reaching the radiative equilibrium. The last 30 years of simulation were

210 used to extract the SST field. This field exhibit the features of reduced zonal and meridional gradients, in accordance with Burls and Fedorov (2014). We refer to this SST field as the "full Pliocene SST". We also ran a pre-industrial control simulation for 170 years, taking the last 30 years to extract the "pre-industrial control" SST field. In order to create a Pliocene SST field for the tropics only ("10 °SN Pliocene SST"), we merged the full Pliocene SST in the tropics to the pre-industrial control SST in the extratropics using

215 $$SST_{10SNPliocene} = fSST_{Pliocene} + (1-f)SST_{Preindustrial} \qquad (1)$$

where

$$f = \exp(-(latitude/10)^6) \qquad (2)$$

with latitude in degrees.

Second, we took the pre-industrial control SST field, the Pliocene SST field, and the 10 °SN Pliocene SST field, ran fixed-

220 SST simulations for each. Note that we use the standard CAM4 model for each simulation (i.e. we do not alter the cloud properties), so that the climate model physics is consistent. Those simulations were run at several CO_2 levels (284.7 ppmv, 300 ppmv and 320 ppmv for the full Pliocene SST; 284.7 ppmv and 300 ppmv for the 10 °SN Pliocene SST). We did so in order to estimate at which CO_2 the atmosphere is in equilibrium with the SST, meaning that the net surface heat flux (F_{net}, Eq. 3) sums at zero. We estimated those CO_2 levels as 309.4 ppmv for the full Pliocene SST and 299.4 ppmv for the 10 °SN

225 Pliocene SST, by linearly interpolation F_{net} as a function of $\log(CO_2)$. F_{net} is computed as:

$$F_{net} = F_{SW} - F_{LW} - F_L - F_S \qquad (3)$$

Where F_{SW} is the net (downward) solar flux, F_{LW} is net net (upward) long-wave flux, F_L is the latent heat flux, and F_S the sensible heat flux, all fluxes at Earth surface. These fixed-SST simulations were run 40 years, and the last 30 years were used to extract F_{net}.

230 Third, we used 0-sum F_{net} from the full and 10 °SN Pliocene SST to derive oceanic Q flux: Q. The Q flux refers to the forcing term of a slab ocean model. It represents the divergence of oceanic heat transport, and directly controls the warming or cooling of the surface ocean, in a slab model. We computed the Q flux for each month of the annual cycle with the following equation:

$$Q(t) = F_{net}(t) - \rho_{wat}c_{p_{wat}}h_{ml}\frac{d(SST)}{dt} + \rho_{ice}L_{fus}h_{ice}\frac{dx_{ice}}{dt} \qquad (4)$$
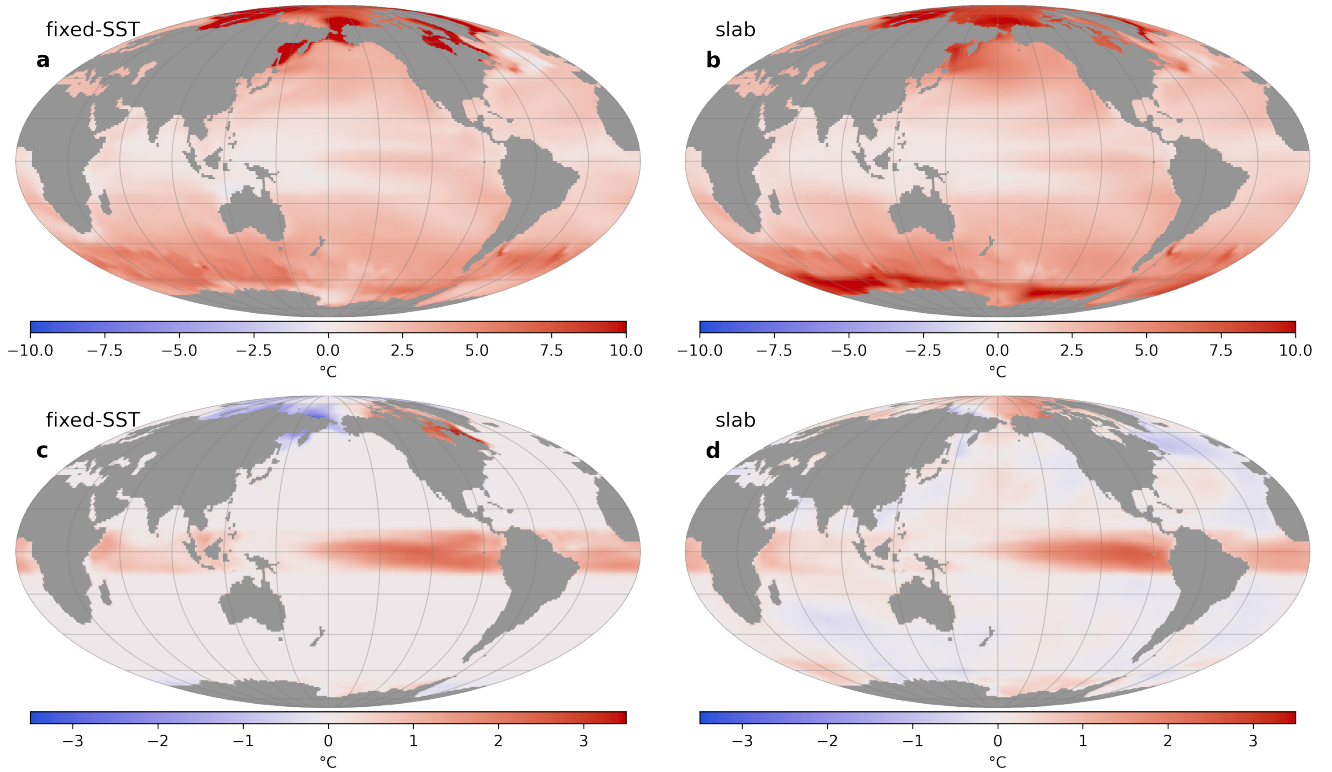
Figure 7. Anomaly of ocean skin temperature (i.e., SST, except on grid points with sea ice) for (a): fixed SST simulation with full Pliocene SST (at 300 ppmv), (b): slab ocean simulation with full Pliocene SST (at 300 ppmv), (c): fixed SST simulation with 10 °SN Pliocene SST (at 309.4 ppmv), and (d): slab ocean simulation with 10 °SN Pliocene SST (at 299.4 ppmv). Note that the scale in (a) and (b) is different from (c) and (d). Map projection and graticules are similar to Fig. 1. In (c), the temperature anomaly is exactly 0 °C outside 10 °S–10 °N, except in polar regions because of the sea-ice surface temperature response to tropical SST forcing. In (d), the temperature anomaly is not perfectly 0 °C outside 10 °S–10 °N, because of inaccuracies in the derivation of the Q flux, but the amplitude of those anomalies is significantly less than within 10 °S–10 °N, with the exception of sea-ice regions.

235 Where ρ_{wat} is the seawater density, $c_{p_{wat}}$ is the seawater heat capacity, h_{ml} is the depth of ocean mixed layer, ρ_{ice} is the density of sea ice, L_{fus} is the latent heat of fusion of water, h_{ice} is the thickness of sea ice, and x_{ice} the fraction of each oceanic grid covered by sea ice. The time derivative was approximated here as the month by month finite difference. The mixed layer depth h_{ml} was taken from the default pre-industrial Q flux forcing (see Methods, section 2.3) and is time-invariant. The SST and ice fraction (x_{ice}) were taken from the Pliocene SST atmosphere-only simulations (full or 10 °SN). More precisely, we computed

240 the anomaly of SST, x_{ice} and F_{net} by subtracting the fields taken from Pliocene SST atmosphere-only simulations to the fields from the pre-industrial control fixed-SST climate run. Noting this subtraction Δ, we actually computed ΔQ as:

$$\Delta Q(t) = \Delta F_{net}(t) - \rho_{wat} c_{p_{wat}} h_{ml} \frac{d(\Delta SST)}{dt} + \rho_{ice} L_{fus} h_{ice} \frac{d(\Delta x_{ice})}{dt} \qquad (5)$$
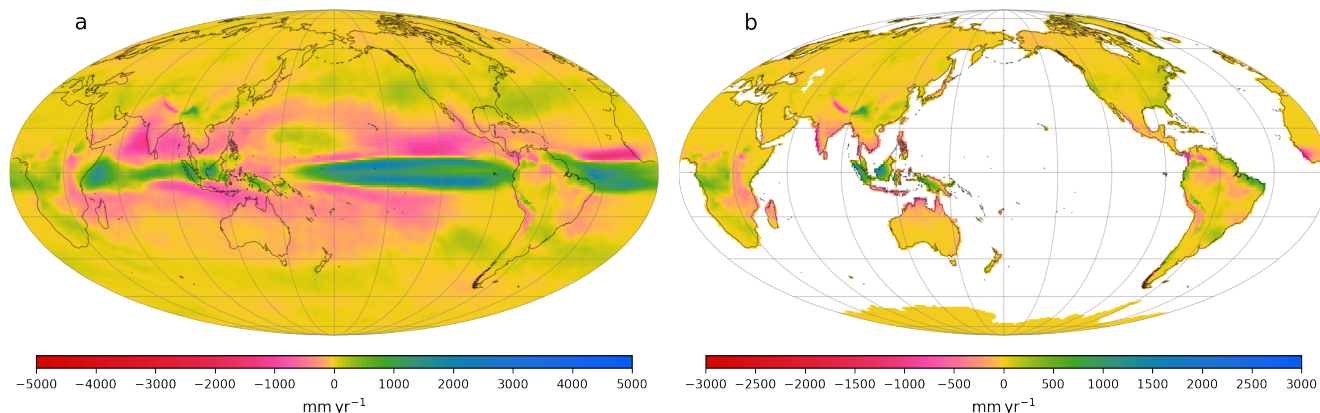
Figure 8. Annual mean climatology of slab ocean simulation with $10\,°SN$ Pliocene SST at $299.4\,\mathrm{ppmv}$ with respect to the pre-industrial control. (a): total precipitation, and (b): continental runoff. Map projection and graticules as in Fig. 1.

With ΔQ thus calculated, the Pliocene Q flux was computed as $Q_{control} + \Delta Q$ (for both full SST or $10\,°\mathrm{N/S}$ SST fields). Using this generated Q flux, we ran climate simulations with the slab ocean version of CESM1.2, at the "standard" CO_2

245   level (309.4 ppmv or 299.4 ppmv, see previous paragraph) and at higher or lower CO_2 (180 ppmv, 200 ppmv, 250 ppmv, 427.1 ppmv and 569.4 ppmv) to encompass the full range of climate warming or cooling, as CO_2 must adjust to balance the geological C cycle. Here again, the standard CAM4 model is used in all instances, so that the climate model physics is consistent.

     The least constrained variable here is the sea-ice thickness (h_{ice}). In the absence of information, as it cannot be retrieved

250   from the fixed SST simulations, we assumed a constant, uniform thickness of $1\,\mathrm{m}$. Despite this crude assumption, the slab ocean simulations (at standard CO_2) reproduce well the SST fields from the original ocean-atmosphere coupled model (see Fig. 7), except in a few local spots, in regions influenced by sea-ice.

     Finally, we note that these estimated CO_2 levels that balance the heat flux in the fixed-SST simulations are different from the C cycle equilibrium CO_2 levels computed by GEOCLIM. The former is done so that the derived Q-flux change does not

255   artificially introduce heat into or out of the ocean. With a slab ocean model, the null F_{net} condition is verified for any CO_2 level, because it is imposed by the Q flux. The latter CO_2 levels computed by GEOCLIM are the ones that balance the geologic C cycle.

3.2.1   Weathering and equilibrium temperature with reduced zonal gradient

In this section, we examine the simulations where the Pliocene SST field is applied in the $10\,°\mathrm{S}$–$10\,°\mathrm{N}$ band ($10\,°SN$ Pliocene

260   SST) with the slab ocean version of CESM.

     The standard CO_2 experiment for this configuration (299.4 ppmv, see previous section) has a Global Mean $2\,\mathrm{m}$ Temperature of $13.67\,°\mathrm{C}$, which is $0.25\,°\mathrm{C}$ warmer than the pre-industrial control (at $284.7\,\mathrm{ppmv}$). The precipitation anomaly (Fig. 8a)
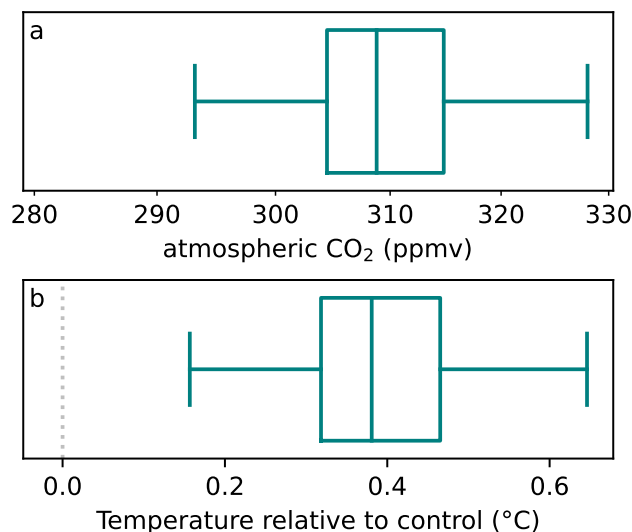
Figure 9. Results for the $10\,°SN$ Pliocene SST GEOCLIM simulation at C cycle equilibrium (i.e., with silicate weathering flux balancing control degassing). (a): atmospheric CO_2 level (logarithmic axis) and (b): anomaly (with respect to pre-industrial simulation) of Global Mean $2\,m$ Temperature. The $0\,°C$ anomaly in (b) is highlighted by a thin grey dotted vertical line. The distribution – shown as a boxplot – represents the ensemble of GEOCLIM parameterizations (similarly to Fig. 4 and 6). The x axis of panel (a) is bounded so that a given CO_2 in panel (a) correspond to the aligned global temperature in panel (b). This with the approximation that the CO_2 is continuously logarithmic (from lower to upper bound), whereas GEOCLIM $\log(CO_2)$-interpolates climate fields between the CO_2 levels – the ones considered here being $250\,ppmv$, $299.4\,ppmv$ and $427.1\,ppmv$. Because of this approximation, the boxplots in (a) and (b) are not perfectly aligned, but this misalignment is negligible.

exhibits a large increase in the eastern Pacific, similar to El Niño events. This increase does not extend southward as much as for observed El Niño conditions (Fig. 1b), likely because we imposed SST perturbation only in the $10\,°S–10\,°N$ band. Instead
265 of drier conditions around the Maritime Continent and wetter conditions in the western Indian ocean characteristic of El Niño, precipitation increases along the equator ($\sim \pm 5\,°$) across the Indian ocean, and extends up to the eastern coast of Borneo over the Maritime Continent. The islands of Borneo, Sulawesi, and New Guinea show a similar pattern of wetter conditions except on their western edge. The tropical Atlantic also shows significant difference with El Niño, as because the imposed SST in the Atlantic is warmer almost uniformly along the equator (Fig. 7 c and d), which favors atmospheric convection. The runoff
270 anomaly (Fig. 8 a) reveals some similarities with the El Niño case (Fig. 1c): a decrease over India and South-East Asia, an increase over China and the eastern side of the Himalaya, an increase in the Andes around the equator, a decrease in the rest of equatorial South America (though the enhanced convection in the Atlantic generates wetter conditions along the Atlantic coast), an increase in the South-east part of South America, and an increase over the Congo basin. The largest discrepancies are found on the Maritime Continent, and the East African rift.
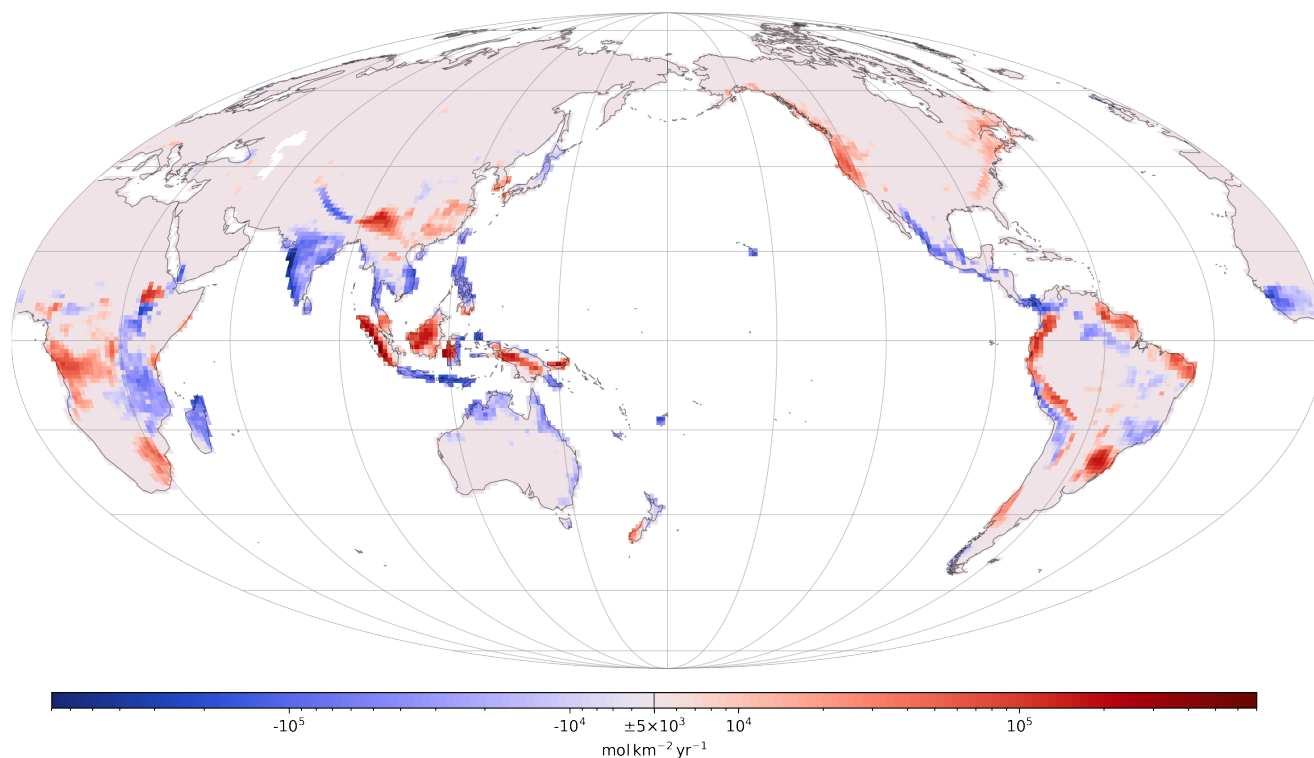
Figure 10. Anomaly of weathering rate of slab ocean climate simulation with $10\,^\circ$SN Pliocene SST at $299.4\,\mathrm{ppmv}$ with respect to pre-industrial control (averaged over the parameter combinations, similarly to Fig. 5).

275   We then used the $10\,^\circ$SN Pliocene SST simulations at several CO_2 levels to compute the equilibrium CO_2, which is the value at which the silicate weathering flux with $10\,^\circ$SN Pliocene SST balances CO_2 degassing. More precisely, we consider that control CO_2 degassing is equal to pre-industrial silicate weathering flux. Therefore, for each selected combination of GEOCLIM parameters (see Methods, section 2.1), we imposed that the silicate weathering flux with $10\,^\circ$SN Pliocene SST is equal to the silicate weathering flux with the same parameter combination in the pre-industrial control simulation (i.e.,

280   computed with climate fields from pre-industrial slab simulation. This "control" weathering is shown on Fig. 4, orange bars.) Figure 9 shows this equilibrium CO_2 (panel a) and the Global Mean $2\,\mathrm{m}$ Temperature corresponding to that CO_2 concentration (panel b). The Pliocene SST (within $10\,^\circ$S–$10\,^\circ$N) generates climatic conditions less favourable for weathering, causing CO_2 to increase, and global temperature to rise by $\sim 0.4\,^\circ$C, which is about twice that estimated using ERA5 reanalysis of El Niño years. This result is consistent with the fact that, in the $10\,^\circ$SN Pliocene SST simulation, the west-to-east Pacific SST difference

285   is reduced by more ($\sim 2\,^\circ$) than in the El Niño years climatology ($\sim 1.5\,^\circ$). Note that, though the climate sensitivity (global temperature difference for a CO_2 doubling) stays the same, there is an offset in the CO_2-temperature relationship, meaning that a CO_2 of $284.7\,\mathrm{ppmv}$ does not correspond to a $0\,^\circ$C temperature anomaly.
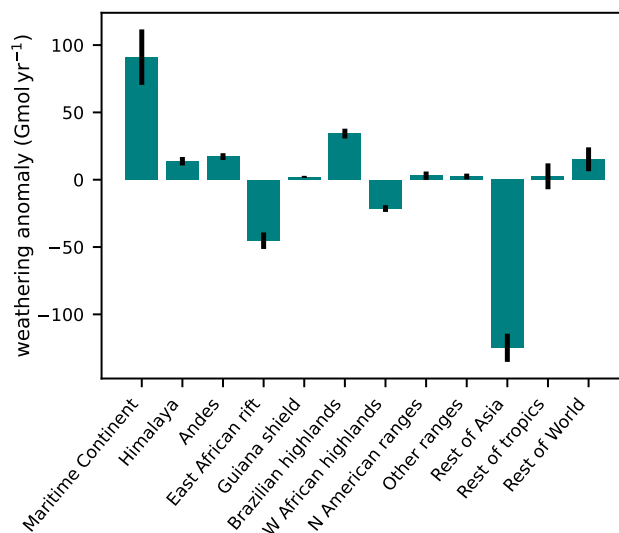
Figure 11. Bar plot of the anomaly of weathering flux of slab ocean climate simulation with $10\,^\circ$SN Pliocene SST at $299.4\,$ppmv with respect to pre-industrial control, integrated over the geographic regions (similarly to Fig. 6).

This decrease of weatherability (or weathering efficiency) can be investigated by looking at the anomaly of silicate weathering rate of $10\,^\circ$SN Pliocene SST at $299.4\,$ppmv with respect to pre-industrial control weathering rate (Fig. 10). Though the global temperature is not the same ($10\,^\circ$SN Pliocene SST is $0.25\,^\circ$C warmer), it still illustrates the causes of this decrease in weatherability. Similar to what was observed with El Niño and La Niña composites (Fig. 5), several positive and negative regional anomalies of weathering, driven by runoff changes, compensate each other, leading to a weak warming. Nevertheless, this warming is consistent over the whole ensemble of parameter combinations. Figure 11 show the integration of the weathering rate anomaly from Fig. 10 over the geographic regions presented Fig. 2. Unlike the El Niño case, the weathering anomaly integrated over the Maritime Continent is positive, and thereby not contributing to the warming. Indeed, there are more increases than decreases in runoff on the Maritime Continent in the $10\,^\circ$SN Pliocene SST simulation. The East African rift also has an opposite behaviour, with a decrease of weathering instead of a slight increase with El Niño. The last main difference concerns the category "rest of Asia", showing a large decrease in weathering. The decrease in runoff in India, and associated weathering decrease, overwhelms the increase in China, whereas those two balance out under modern El Niño conditions.

In summary, applying our estimation of Pliocene SST in the $10\,^\circ$S–$10\,^\circ$N band – whose main feature is a flattening the tropical Pacific zonal gradient – generates a similar weatherability decrease and global warming to that estimated from El Niño (section 3.1.2), though approximately twice as large. However, the mechanisms of that weatherability decrease are different, due to differences in the regional patterns of simulated runoff.
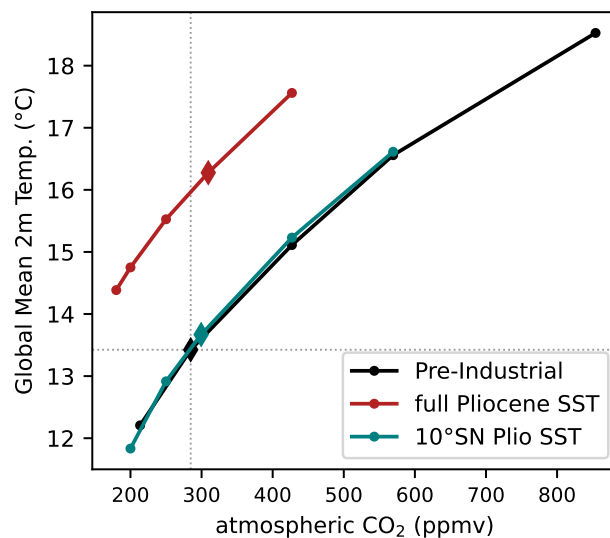
Figure 12. Global Mean $2\,\mathrm{m}$ Temperature (GMST) plotted against atmospheric CO_2 level for the 3 series of slab ocean GCM simulations: pre-industrial boundary conditions, full Pliocene SST and $10\,°\mathrm{SN}$ Pliocene SST. Each dot represents an actual simulation, the diamonds correspond to the "standard" CO_2 levels ($284.7\,\mathrm{ppmv}$ for pre-industrial, see previous section for Pliocene SST). Control (pre-industrial) CO_2 level and GMST are highlighted by the horizontal and vertical thin grey dotted lines.

3.2.2 Simulation with full Pliocene Sea Surface Temperature

305 We now examine the slab ocean climate simulations where the full Pliocene SST field is applied. The most noticeable feature of the full Pliocene SST simulation is its mean temperature anomaly. As shown in Fig. 12, for any given CO_2 level, the full Pliocene SST slab ocean simulation is about $2.5\,°\mathrm{C}$ warmer than its counterpart with pre-industrial boundary conditions.

These warmer conditions at a given CO_2 level can be explained by analysing the components of the radiative budget. Figure 13 shows the comparison between the full Pliocene SST simulation and pre-industrial simulations interpolated at $309.4\,\mathrm{ppmv}$
310 (same CO_2 level than Pliocene SST simulation) and at $538.3\,\mathrm{ppmv}$ (CO_2 level at which the Global Mean $2\,\mathrm{m}$ Temperature equals the one of the Pliocene SST simulation). A significant signal of the full Pliocene SST simulation can be found in the net solar radiative flux at top of atmosphere (Fig. 13 a and e). There are 2 peaks of incoming radiation in the tropics (around $5\,°\mathrm{N}$ and $10\,°\mathrm{S}$, Fig. 13e), that do not appear just by raising CO_2 with pre-industrial boundary conditions. Such tropical peaks are caused by reduced cloudiness (Fig. 13 d and h), due to less intense convection because of the reduced zonal temperature
315 gradient, lowering Earth visible albedo. Indeed, the cloud contribution to the peaks, estimated by the difference "full sky" minus "clear sky" (dashed lines in Fig. 13e) is almost 100% of the signal. Another peak in incoming solar radiation can be seen around $40\,°$ N or S Fig. (13e) and corresponds to a poleward shift in cloudiness at those latitudes (Fig. 13d), mostly discernable in the Southern Hemisphere. This feature, however, is also found in the pre-industrial simulation at $538.3\,\mathrm{ppmv}$, and may be a mere consequence of rising global temperature, though its amplitude is higher in the full Pliocene SST simulation. More solar
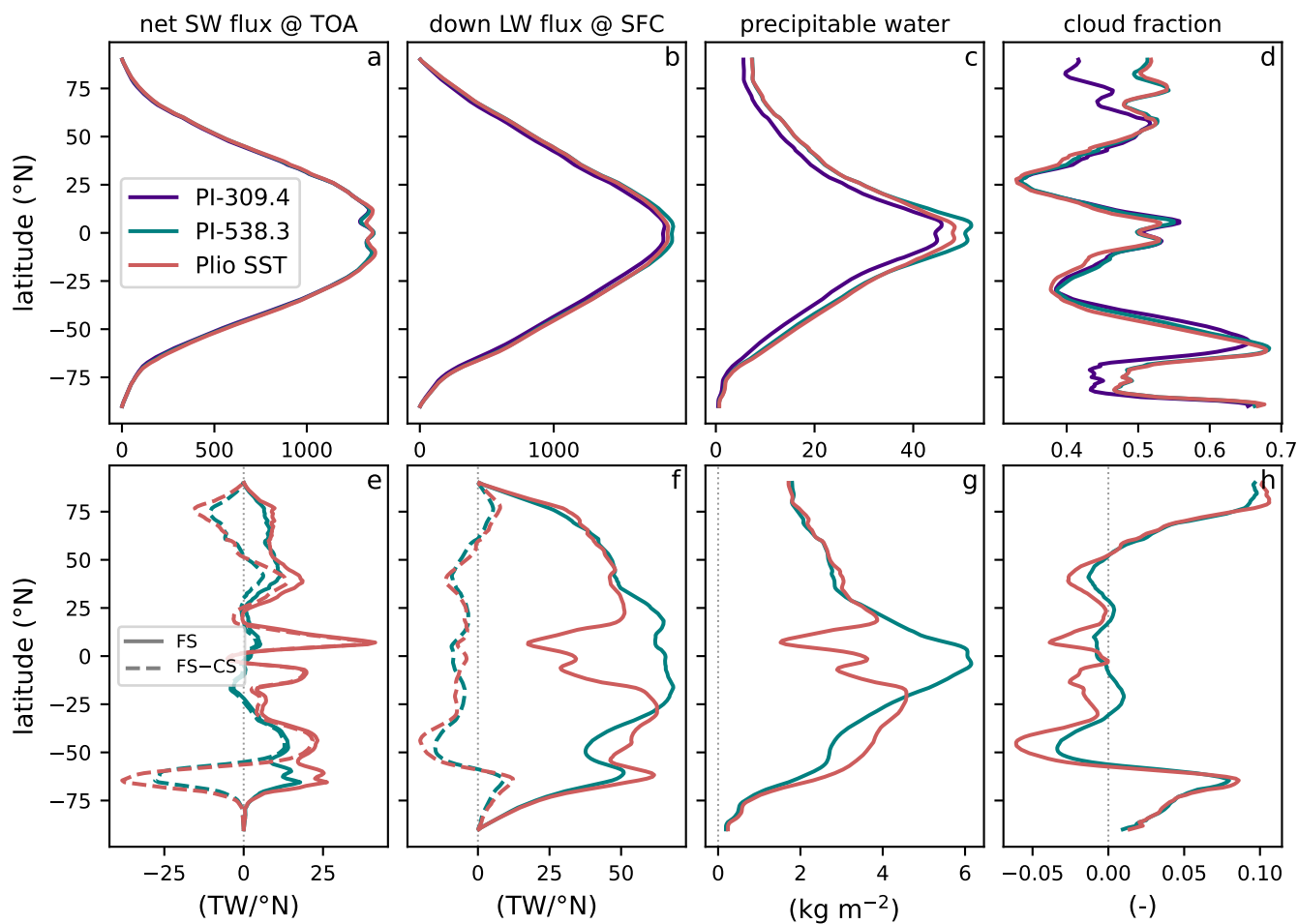
Figure 13. Comparison of zonal annual mean fluxes and climatology for the three simulations which are: pre-industrial boundary conditions $\log(CO_2$-interpolated at 309.4 ppmv (indigo) or at 538.3 ppmv (teal), and full Pliocene SST (at 309.4 ppmv). (a): zonally-integrated net (incoming minus outgoing) solar (SW) radiative flux at top of atmosphere (TOA), (b): zonally-integrated downwelling long-wave (LW) radiative flux at Earth surface (SFC), (c): zonally-averaged total precipitable water (vertically integrated), (d): zonally-averaged total cloud fraction (vertically integrated). All variables are annual mean climatology. (e), (f), (g) and (h) are similar to (a), (b), (c) and (d) (respectively) but with 309.4 ppmv pre-indutsrial subtracted, the thin vertical grey dashed line highlights zero anomaly. The dashed color lines in (e) and (f) shows the difference full sky (SF) minus clear sky (CS), illustrating the contribution from clouds. The solid lines (full sky) are the regular values, as in (a) and (b). The "0 anomaly" in panels (e)–(h) is highlighted by a thin grey dotted vertical line. The color code holds for the entire figure.

320   radiation also enters at high latitude in the Pliocene simulations relative to the pre-industrial control, due to the retreat of sea ice, also lowering visible albedo. Though it is is countered by increase in cloudiness (Fig. 13d and h), as can be seen in the cloud contribution in Fig. 13e, the net effect is still positive. Similarly to the peak at $40°$ N or S, this phenomenon is also present in
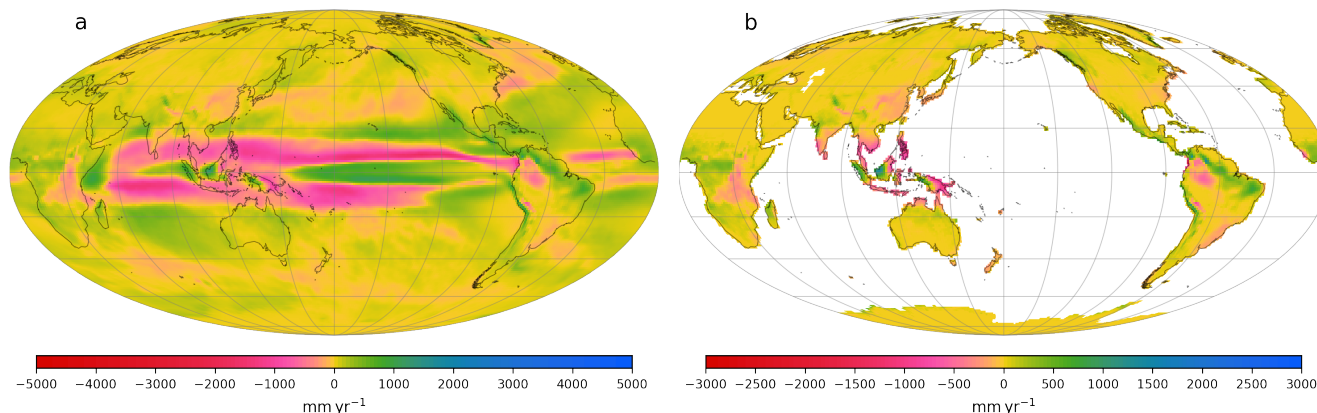
Figure 14. Annual mean climatology of the slab ocean simulation with full Pliocene SST at 309.4 ppmv with respect to the pre-industrial control $\log(CO_2)$-interpolated at 358.3 ppmv. This last CO_2 level was chosen so that the two simulations in the difference have the same Global Mean 2 m Temperature. (a): total precipitation, and (b): continental runoff. Map projection and graticules as in Fig. 1.

the pre-industrial 538.3 ppmv simulation, but strengthened in the Pliocene SST simulation. On global average, the net solar radiation forcing of the full Pliocene simulation (with respect to pre-industrial at same CO_2) is $+3.9 \, \text{W m}^{-2}$, the tropical part alone being $+1.0$ equivalent W m^{-2} (equivalent if spread on the whole Earth). The latitude profile of downwelling long-wave radiation at Earth surface also shows some variations (Fig. 13 b and f), essentially following the anomaly of water vapour (Fig. 13 c and g). The reduced meridional temperature gradient in the full Pliocene SST simulation is responsible for less water vapour in the tropics, and more water vapour in the extra-tropics, compared to the pre-industrial simulation at same mean temperature (Fig. 13g), though it is mostly visible in the Southern hemisphere. The downwelling long-wave radiation at the surface exhibits the same behaviour. The more significant drops in the tropics (still compared to the pre-industrial simulation at same mean temperature) is likely due to the reduced Hadley circulation. The averaged downwelling long-wave flux anomaly is not so different between the Pliocene SST simulation and the pre-industrial one at 538.3 ppmv (respectively, $+14.0$ and $+15.8 \, \text{W m}^{-2}$), both seem to be a consequence of warmer atmosphere (and amplifier, through a positive feedback loop). In summary, we can conclude that the main warming causes of the full Pliocene SST simulation are the decrease in cloudiness in the tropics, due to a weaker convection and Hadley circulation, combined with a decrease of cloudiness around 40 degree N and S and of sea ice at high latitude, these last two also being part of a positive feedback enhancing the "initial" warming.

In term of precipitation, it is easier to compare the full Pliocene SST simulation with the pre-industrial simulation $\log(CO_2)$-interpolated at the same global temperature, to cancel the effect of increased precipitation with global warming. This precipitation (and runoff) difference is shown on Fig. 14. A redistribution of precipitation, with a decrease in the tropics and an increase in the extra-tropics can be observed, superimposed to the anomalies already observed in the $10\,°\text{SN}$ Pliocene SST simulation (Fig. 8): increase in the eastern tropical Pacific and on the western boundaries of tropical Indian and Atlantic oceans. The results are different for land precipitation. Despite the reduced meridional temperature gradient, precipitation and runoff mostly increase in tropical Africa and South America, with the exception of the western part of this Amazon basin and the
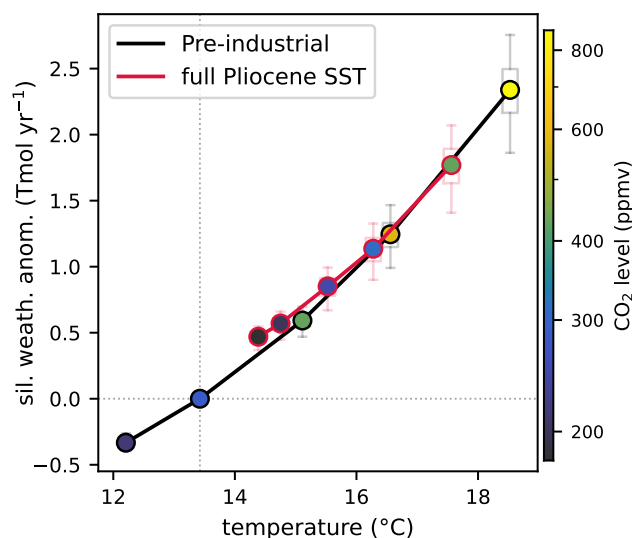
Figure 15. Total silicate weathering fluxes anomaly (with respect to pre-industrial control) plotted against Global Mean $2\,\mathrm{m}$ Temperature (GMST), for the pre-industrial and the full Pliocene SST simulations (each of those repeated at 5 different CO_2 levels, see also Table 1). Each dot represents a single simulation, at fixed CO_2, its level being indicated with the colorscale. The semi-transparent boxplots show, for each simulation, the variability of weathering across the parameter combinations. Null weathering anomaly and pre-industrial GMST are highlighted by the vertical and horizontal thin grey dotted lines.

East African rift, where a drying tendency was already observed in the $10\,°\mathrm{SN}$ Pliocene SST simulation. This goes against
345   our initial hypothesis, based on the "wet gets dryer, dry gets wetter" feature from Burls and Fedorov (2017). The Maritime
Continent exhibits a contrasting behaviour, with wetter conditions on the western sides of the most equatorial islands, and
dryer conditions on their eastern side. Such behaviour was also present in the $10\,°\mathrm{SN}$ Pliocene SST simulation, with a larger
precipitation increase on the western sides, but is highlighted here because the anomaly is computed with respect to the pre-
industrial simulation at $538.3\,\mathrm{ppmv}$ instead of $284.7\,\mathrm{ppmv}$: the increase on the eastern sides is less than the roughly uniform
350   increase due to higher CO_2, whereas the increase on the western sides is larger. On global average, precipitation increase by
$15\,\mathrm{mm\,yr^{-1}}$ and continental runoff increase by $16\,\mathrm{mm\,yr^{-1}}$.

    The offset in global temperature for a given CO_2 level (in full Pliocene SST simulations, with respect to pre-industrial ones)
poses a technical problem: to go back down to pre-industrial temperature, with full Pliocene SST, CO_2 needs to be lowered
to $\sim 140\,\mathrm{ppmv}$. Such CO_2 levels are unrealistically low and are even lower than those during Pleistocene glacial maxima.
355   Moreover, at this CO_2 level, plant stomates cease to operate normally in the land model of CESM, with huge consequences
on the hydrologic cycle. Shut stomates behaviour contrasts with the regular tendency for stomates is to be more open at lower
CO_2 and severely reduces transpiration, eventually leading to increased global runoff, though the mean temperature is lower.
Therefore, it is not possible to properly simulate silicate weathering with GEOCLIM. Increased runoff would lead to increased
weathering at lower CO_2 (thereby killing the negative feedback); on the other hand, the fact that plants cannot survive would
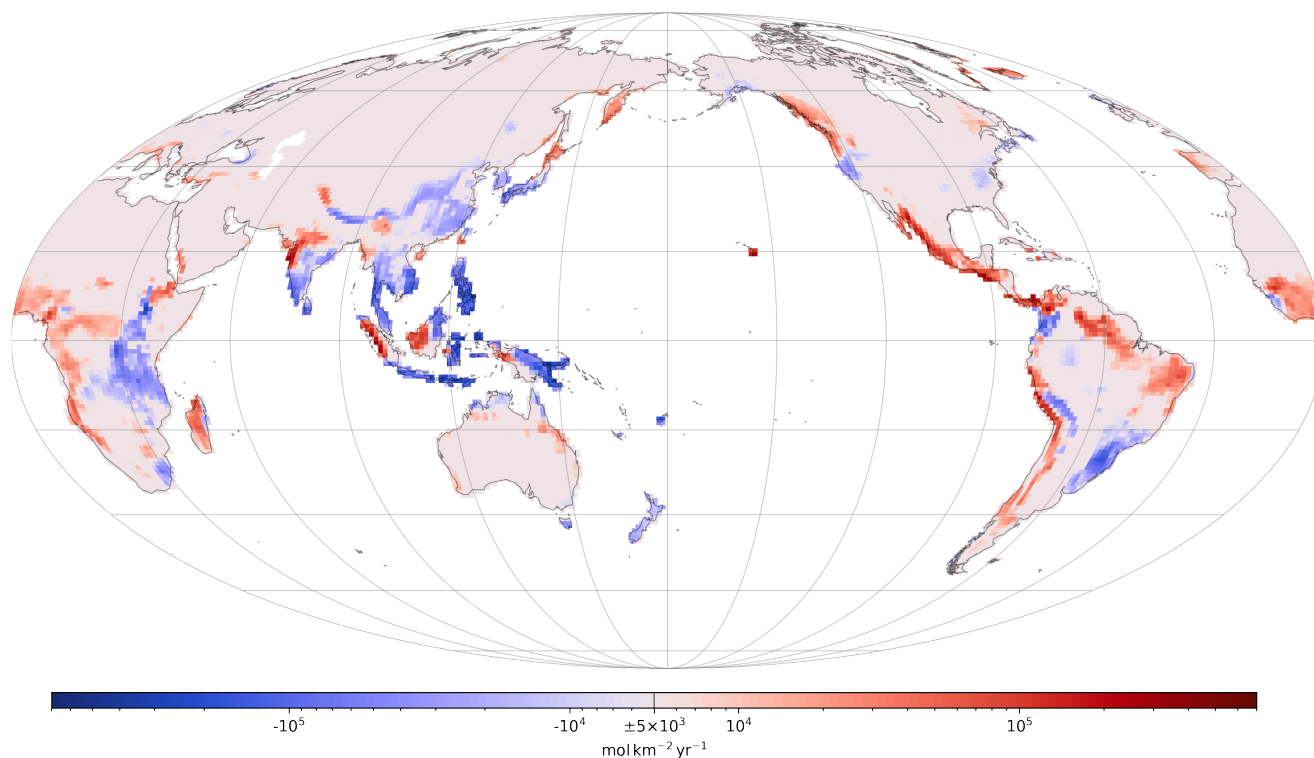
Figure 16. Similar to Fig. 10, anomaly of weathering rate of slab ocean climate simulation with full Pliocene SST at $309.4\,\mathrm{ppmv}$. The anomaly is computed with respect to pre-industrial simulation interpolated at $358.3\,\mathrm{ppmv}$ (see Fig. 14).

360 undermine weathering, as plant roots are a major weathering agent. For this reason, we cannot perform the inversion to compute the equilibrium CO_2 where silicate weathering flux balances pre-industrial degassing. We instead analyse the weathering fluxes at fixed CO_2.

Figure 15 shows the silicate weathering fluxes of the pre-industrial and full Pliocene SST simulations. Despite the higher continental runoff, compared to the pre-industrial simulation at same global temperature, the full Pliocene SST temperature-
365 weathering curve and the pre-industrial curve are superimposed, except for very low CO_2 ($< 200\,\mathrm{ppmv}$) Pliocene simulations. This result means that Pliocene SST does not generate any significant increase or decrease of weatherability, save perhaps at low CO_2, which is likely due to CO_2-plants interaction. If carbon cycle was left to reach balance, CO_2 would decrease until temperature is back around pre-industrial one, although that temperature value is hard to estimate given the uncertainties on weathering at low CO_2.

370 The fact that higher mean runoff does not lead to higher weatherability means that the regions where runoff decrease matter more in term of weathering. Comparing the full Pliocene SST simulation to the pre-industrial interpolated at the same global temperature ($538.3\,\mathrm{ppmv}$) reveals weathering decreases in the almost all of the South-East Asia, India, China, the East African
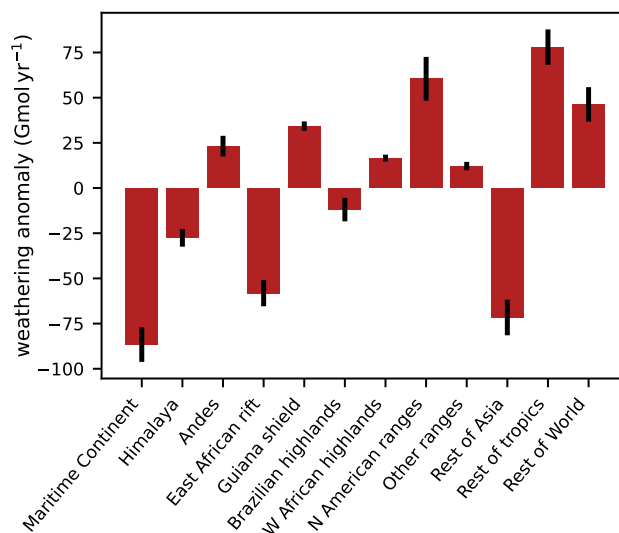
Figure 17. Bar plot of the anomaly of weathering flux of the slab ocean climate simulation with full Pliocene SST at $299.4\,\mathrm{ppmv}$ with respect to pre-industrial control interpolated at $358.3\,\mathrm{ppmv}$ (see text and Fig. 14, and integrated over the geographic regions (similarly to Fig. 6).

rift, and even the Brazilian highlands and the Himalaya (Fig. 16). The combined decrease of those regions – mostly the first 4 – is enough to counteract the increase in rest of tropical land masses (Africa and South America), and along most the of American Cordillera (from the Andes to the Cascade range, Fig. 16) as shown in Figure 17.

4 Discussion

Our results emphasize the different effects on silicate weathering of meridional and tropical zonal gradient of temperature, that are characteristic of Pliocene warmth, according to temperature proxies and mechanistic connection between meridional and zonal SST gradients (Fedorov et al., 2015).

An estimate of the consequences of Pliocene permanent El Niño using reanalysis of modern El Niño events suggests a reduction of global weatherability by $1.7\,\%$, that would correspond to a $\sim 0.23\,\mathrm{°C}$ warming, assuming a simple linear weathering sensitivity. Climate simulations with an estimated reconstruction of Pliocene SST in the $10\,\mathrm{°S}$–$10\,\mathrm{°N}$ band indicate a $\sim 0.4\,\mathrm{°C}$ warming relative to present-day conditions, but arising from different mechanisms. While El Niño reanalysis emphasized the role of the Maritime Continent in this warming, through reduced weathering flux, climate simulations suggest in contrast higher weathering flux in the Maritime Continent, offsetting the warming generated by weathering decrease in mainland South-East Asia, India and the East African rift. Determining which of the two scenarios is the most reliable is not an easy task. Climate models contain biases, in particular for simulating precipitation. The way precipitation on the Maritime Continent is affected by SST changes, in the CESM model, may not be accurate. One potential cause could be the poorly simulated diurnal cycle in

atmospheric convection on those islands. On the other hand, modern El Niño are transient events, lasting a few months, with a
peak in winter, and not subject to the constraint of balancing the Earth radiative budget. These features differ from stationary
(permanent) El Niño conditions. There is no guarantee that El Niño events are a perfect analog of Pliocene permanent El Niño.
Differences in tropical climate dynamics need to be consider in particular as we found significant differences between El Niño
reanalysis and our $10\,°S$–$10\,°N$ Pliocene SST experiments.

Nonetheless, the results agree on a moderate warming effect of permanent El Niño resulting from reduced global weather-
ability. However, this effect is not seen when the entire estimation of Pliocene SST is applied to the climate model. Further
complications arise from the radiative budget of the Pliocene SST simulation, that is $\sim 2.5\,°C$ than pre-industrial for a given
CO_2 level. This temperature shift is mostly caused by lower visible albedo due to fewer clouds in the tropics, as well as a
poleward shift in the mid-latitude peak of cloudiness, and reduced sea-ice. If flatter meridional temperature gradient is the
result of higher global temperature (due to higher CO_2), a direct consequence would be that climate sensitivity to CO_2 is much
higher than current estimations. This raise the question of how representative of Pliocene SST is our reconstruction using Burls
and Fedorov (2014)'s method – modifying clouds visible albedo.

Overall, counteracting regional increase and decrease of land precipitation tends to balance each other out in a permanent El
Niño, though uncertainties remain on the overall net effect. Additionally, the reduced meridional SST gradient seems to cancel
the warming potential of reduced tropical zonal SST gradient by increasing mean precipitation and continental runoff, and no
significant weatherability decrease due to dryer tropics is observed.

5 Conclusions

Long-term cooling of Earth's climate from the mid-Miocene to the present associated with decreasing CO_2 likely resulted
from increase weatherability (e.g., Park et al., 2020), decrease outgassing (e.g., Herbert et al., 2022), or a combination of
the two. Superimposed on this long-term trend are large changes in climate dynamics whose impact on regional climatology
could plan an important role in processes such as the growth of Northern Hemisphere ice sheets (e.g., Molnar and Cronin,
2015). Additionally, regional changes in precipitation and runoff could alter silicate weathering with resulting implications for
geologic carbon sequestration and steady-state CO_2 levels. This phenomenon can be called "weatherability pattern effect", by
analogy with climate sensitivity. In this contribution, we investigated the 'weatherability pattern effect" due to SST gradients.
We both put forward and evaluate the hypothesis that the transition from a Pliocene permanent El Niño climate to a modern El
Niño-Southern Oscillation climate could be associated with an increase in weatherability due to increases in runoff in chemical
weathering hotspots. We find support for this hypothesis through running chemical weathering models utilizing El Niño climate
as in reanalysis data and through imposing tropical Pliocene SST – with complexities emerging in seeking to utilize a full
Pliocene SST boundary condition. Overall, the difference of a permanent El Niño climate state on global silicate weathering
and resulting simulated differences in global temperature are relatively minor given compensating regions of enhanced versus
diminished chemical weathering. Significant differences are found in the weathering patterns of the different experiments,

particularly on tropical weathering hotspots. These results highlight the importance and the uncertainties of tropical climate and associated dynamics on Earth's long-term climate cycle.

Code availability. All code associated with this study can be found on Github (https://github.com/piermafrost/GEOCLIM-dynsoil-steady-state/tree/PEN) that is also archived on Zenodo (generate archive at time of revisions)

425   *Data availability.* All climate and GEOCLIM simulations used for this study are available on the dataset https://doi.org/10.6078/D11H7D

Author contributions. P.M. and J.C.H.C. conceived the experiments and ran the climate simulations, P.M. ran the GEOCLIM simulations, wrote the original manuscript draft, and drafted the figures. J.C.H.C. and N.L.S.-H. contributed to manuscript writing. J.C.H.C and N.L.S.-H. acquired funding and supervised project research.

Competing interests. The authors declare no conflict of interest

430   *Acknowledgements.* Research was supported by NSF Frontier Research in Earth Science grant EAR-1925990 awarded to N.L.S.-H. and J.C.H.C. We thank Natalie Burls for useful discussions on climate dynamics and guidance on the design and interpretation of the climate simulations. We dedicate this work to the memory of our dear colleague and friend Sarah White, whose work on permanent El Niño and its impacts inspired this manuscript.

References

435   Berner, R. A., Lasaga, A. C., and Garrels, R. M.: The carbonate-silicate geochemical cycle and its effect on atmospheric carbon dioxide over
      the past 100 million years, American Journal of Science, 283, 641–683, https://doi.org/10.2475/ajs.283.7.641, 1983.

      Brierley, C. M. and Fedorov, A. V.: Relative importance of meridional and zonal sea surface temperature gradients for the on-
      set of the ice ages and Pliocene-Pleistocene climate evolution: SST GRADIENTS AND ICE AGES, Paleoceanography, 25,
      https://doi.org/10.1029/2009PA001809, 2010.

440   Brierley, C. M., Fedorov, A. V., Liu, Z., Herbert, T. D., Lawrence, K. T., and LaRiviere, J. P.: Greatly Expanded Tropical Warm Pool and
      Weakened Hadley Circulation in the Early Pliocene, Science, 323, 1714–1718, https://doi.org/10.1126/science.1167625, 2009.

      Burls, N. J. and Fedorov, A. V.: What Controls the Mean East–West Sea Surface Temperature Gradient in the Equatorial Pacific: The Role
      of Cloud Albedo, Journal of Climate, 27, 2757–2778, https://doi.org/10.1175/JCLI-D-13-00255.1, 2014.

      Burls, N. J. and Fedorov, A. V.: Wetter subtropics in a warmer world: Contrasting past and future hydrological cycles, Proceedings of the
445   National Academy of Sciences, 114, 12 888–12 893, https://doi.org/10.1073/pnas.1703421114, 2017.

      Cannariato, K. G. and Ravelo, A. C.: Pliocene-Pleistocene evolution of eastern tropical Pacific surface water circulation and thermocline
      depth, Paleoceanography, 12, 805–820, https://doi.org/10.1029/97PA02514, 1997.

      Dessert, C., Dupré, B., Gaillardet, J., François, L. M., and Allègre, C. J.: Basalt weathering laws and the impact of basalt weathering on the
      global carbon cycle, Chemical Geology, 202, 257–273, https://doi.org/10.1016/j.chemgeo.2002.10.001, 2003.

450   Farr, T. G., Rosen, P. A., Caro, E., Crippen, R., Duren, R., Hensley, S., Kobrick, M., Paller, M., Rodriguez, E., Roth, L., Seal, D., Shaffer,
      S., Shimada, J., Umland, J., Werner, M., Oskin, M., Burbank, D., and Alsdorf, D.: The Shuttle Radar Topography Mission, Reviews of
      Geophysics, 45, RG2004, https://doi.org/10.1029/2005RG000183, 2007.

      Fedorov, A. V., Dekens, P. S., McCarthy, M., Ravelo, A. C., deMenocal, P. B., Barreiro, M., Pacanowski, R. C., and Philander, S. G.: The
      Pliocene Paradox (Mechanisms for a Permanent El Niño), Science, 312, 1485–1489, https://doi.org/10.1126/science.1122666, 2006.

455   Fedorov, A. V., Brierley, C. M., Lawrence, K. T., Liu, Z., Dekens, P. S., and Ravelo, A. C.: Patterns and mechanisms of early Pliocene
      warmth, Nature, 496, 43–49, https://doi.org/10.1038/nature12003, 2013.

      Fedorov, A. V., Burls, N. J., Lawrence, K. T., and Peterson, L. C.: Tightly linked zonal and meridional sea surface temperature gradients over
      the past five million years, Nature Geoscience, 8, 975–980, https://doi.org/10.1038/ngeo2577, 2015.

      Gabet, E. J. and Mudd, S. M.: A theoretical model coupling chemical weathering rates with denudation rates, Geology, 37, 151–154,
460   https://doi.org/10.1130/G25270A.1, 2009.

      Gaillardet, J., Dupré, B., Louvat, P., and Allègre, C. J.: Global silicate weathering and CO2 consumption rates deduced from the chemistry
      of large rivers, Chemical Geology, 159, 3–30, https://doi.org/10.1016/S0009-2541(99)00031-5, 1999.

      Hartmann, J. and Moosdorf, N.: The new global lithological map database GLiM: A representation of rock properties at the Earth surface,
      Geochemistry, Geophysics, Geosystems, 13, https://doi.org/10.1029/2012GC004370, 2012.

465   Herbert, T. D., Dalton, C. A., Liu, Z., Salazar, A., Si, W., and Wilson, D. S.: Tectonic degassing drove global temperature trends since 20
      Ma, Science, 377, 116–119, https://doi.org/10.1126/science.abl4353, 2022.

      Hersbach, H., Bell, B., Berrisford, P., Biavati, G., Horányi, A., Muñoz Sabater, J., Nicolas, J., Peubey, C., Radu, R., Rozum, I., Schep-
      ers, D., Simmons, A., Soci, C., Dee, D., and Thépaut, J.-N.: ERA5 monthly averaged data on single levels from 1979 to present,
      https://doi.org/10.24381/CDS.F17050D7, type: dataset, 2019.

470 Langenbrunner, B.: The pattern effect and climate sensitivity, Nature Climate Change, 10, 977–977, https://doi.org/10.1038/s41558-020-00946-y, 2020.

Maffre, P., Ladant, J.-B., Moquet, J.-S., Carretier, S., Labat, D., and Goddéris, Y.: Mountain ranges, climate and weathering. Do orogens strengthen or weaken the silicate weathering carbon sink?, Earth and Planetary Science Letters, 493, 174–185, https://doi.org/10.1016/j.epsl.2018.04.034, 2018.

475 Maher, K. and Chamberlain, C. P.: Hydrologic Regulation of Chemical Weathering and the Geologic Carbon Cycle, Science, 343, 1502–1504, https://doi.org/10.1126/science.1250770, 2014.

Molnar, P. and Cronin, T. W.: Growth of the Maritime Continent and its possible contribution to recurring Ice Ages: Maritime Continent Growth and Ice Ages, Paleoceanography, 30, 196–225, https://doi.org/10.1002/2014PA002752, 2015.

Muñoz Sabater, J.: ERA5-Land monthly averaged data from 2001 to present, https://doi.org/10.24381/CDS.68D2BB30, type: dataset, 2019.

480 Oliva, P., Viers, J., and Dupré, B.: Chemical weathering in granitic environments, Chemical Geology, 202, 225–256, https://doi.org/10.1016/j.chemgeo.2002.08.001, 2003.

Park, Y., Maffre, P., Goddéris, Y., Macdonald, F. A., Anttila, E. S. C., and Swanson-Hysell, N. L.: Emergence of the Southeast Asian islands as a driver for Neogene cooling, Proceedings of the National Academy of Sciences, 117, 25 319–25 326, https://doi.org/10.1073/pnas.2011033117, 2020.

485 Ravelo, A. C.: The Role of the Tropical Oceans on Global Climate During a Warm Period and a Major Climate Transition, Oceanography, 17, 32–41, https://doi.org/10.5670/oceanog.2004.28, 2004.

Shukla, S. P., Chandler, M. A., Jonas, J., Sohl, L. E., Mankoff, K., and Dowsett, H.: Impact of a permanent El Niño (El Padre) and Indian Ocean Dipole in warm Pliocene climates, Paleoceanography, 24, n/a–n/a, https://doi.org/10.1029/2008PA001682, 2009.

Trenberth, K. E. and Stepaniak, D. P.: Indices of El Niño Evolution, JOURNAL OF CLIMATE, 14, 5, https://doi.org/10.1175/1520-0442(2001)014<1697:LIOENO>2.0.CO;2, 2001.

490 Urey, H. C.: On the Early Chemical History of the Earth and the Origin of Life, Proceedings of the National Academy of Sciences, 38, 351–363, https://doi.org/10.1073/pnas.38.4.351, 1952.

Walker, J. C. G., Hays, P. B., and Kasting, J. F.: A negative feedback mechanism for the long-term stabilization of Earth's surface temperature, Journal of Geophysical Research, 86, 9776, https://doi.org/10.1029/JC086iC10p09776, 1981.

495 Wara, M. W., Ravelo, A. C., and Delaney, M. L.: Permanent El Niño-Like Conditions During the Pliocene Warm Period, Science, 309, 758–761, https://doi.org/10.1126/science.1112596, 2005.

West, A. J.: Thickness of the chemical weathering zone and implications for erosional and climatic drivers of weathering and for carbon-cycle feedbacks, Geology, 40, 811–814, https://doi.org/10.1130/G33041.1, 2012.